Interplay between single-particle and collective degrees of freedom in the excitation of the low-lying states in ^{140}Ce

W. Kim,[1] B. L. Miller,[2,*] J. R. Calarco,[1] L. S. Cardman,[2] J. P. Connelly,[1,†] S. A. Fayans,[5] B. Frois,[3] D. Goutte,[3] J. H. Heisenberg,[1] F. W. Hersman,[1] V. Meot,[3] T. E. Milliman,[1] P. Mueller,[2] C. N. Papanicolas,[2] A. P. Platonov,[5] V. Yu. Ponomarev,[4] and J. E. Wise[1,‡]

[1]*Department of Physics, University of New Hampshire, Durham, New Hampshire 03824*

[2]*Department of Physics and Nuclear Physics Laboratory, University of Illinois at Urbana-Champaign, 1110 W. Green Street, Urbana, Illinois 61801*

[3]*Département de Physique Nucléaire et de Hautes Energies, Centre d'Etudes Nucléaires de Saclay, 91191 Gif-sur-Yvette CEDEX, France*

[4]*Laboratory of Theoretical Physics, Joint Institute for Nuclear Research, Dubna Head Post Office, P.O. Box 79, SU-101000 Moscow, Russia*

[5]*I. V. Kurchatov Institute of Atomic Energy, Moscow 123182, Russia*

(Received 25 October 1991)

Differential cross sections for electron scattering from ^{140}Ce have been measured for excitation energies less than 3.3 MeV over a range of effective momentum transfer of 0.4 to 3.1 fm^{-1}. The data have been analyzed to extract transition charge densities. These densities are interpreted in terms of a quasiparticle-phonon model and self-consistent finite Fermi system theory to disentangle the collective and noncollective modes of excitation.

PACS number(s): 25.30.Dh, 21.10.Pc, 21.60.Cs, 27.60.+j

I. INTRODUCTION

Electron scattering is well suited for examining the spatial properties of nuclear wave functions due to the purely electromagnetic character of the reaction mechanism and the well-understood relationship between the measured cross section and the nuclear charge and current densities. The ground-state charge and transition charge densities of the nucleus provide the meeting ground between theory and experiment. Shape differences in these densities make it possible to discriminate between collective and noncollective modes of excitation for transitions of the same multipolarity.

Nuclei in the mass region $N=82$ near the partial proton shell closure of $Z=58$ provide attractive cases for the investigation of certain aspects of nuclear structure by electron scattering. One of the goals in this experiment was to test various nuclear structure calculations available in this region by comparing their predictions to transition charge densities of low-lying collective excitations.

Earlier inelastic electron-scattering measurements [1] from magic nuclei unambiguously revealed the surface nature of the low-lying collective states of natural parity. Such behavior was predicted by structure calculations employing both the Hartree-Fock (HF) approach with effective forces [2] and the finite Fermi system (FFS) theory using the coordinate representation technique for calculation of the nuclear response function [3–5].

Efforts have been made to disentangle the contributions of collective and noncollective modes of excitation for transitions of the same multipolarity. A comparison of low-lying quadrupole excitations in ^{88}Sr, ^{89}Y, and ^{90}Zr established [6] the strong single-particle nature of these states, which had previously been thought to be collective vibrations. Recently, the low-lying states in ^{142}Nd have been investigated by inelastic electron scattering [7,8], and it has been found that the extracted transition charge densities indicate a quite different microscopic structure for these states. On the basis of a quasiparticle-phonon approach, it has been shown that this difference can be understood as arising from the interplay between collective and single-particle excitation modes. The comparison of ^{142}Ce with ^{142}Nd has indicated that the two additional neutrons above the closed shell $N=82$ strongly increase the interplay between different components in the wave functions of excited states [9].

Previous electron-scattering experiments on ^{140}Ce have been restricted to the low-momentum-transfer region ($q_{\rm eff} \leq 0.6$ fm^{-1}). Pitthan [10] has probed the low-lying region, while more recently Richter and collaborators [11] have focused on the high-excitation region (6.0–11.5 MeV) searching for $M1/M2$ strength. We have presented in a separate paper [12] the results of a search for high-spin states in ^{140}Ce. We reported the identification of a 12^- state at an excitation energy of 6.31 MeV in ^{140}Ce; this transition was found to have only 8% of the calculated single-particle strength. The absence of strong transverse excitations was interpreted as evidence for fragmentation of the single-particle strength.

We report here the results of the same high-resolution electron-scattering measurements [12] concerning the

*Present address: Kuck and Associates, 1906 Fox Drive, Champaign, IL 61820.

†Present address: Department of Physics, Catholic University of America, Washington, DC 20064.

‡Present address: Nuclear Physics Laboratory, University of Colorado, Boulder, Colorado 80309-0390.

low-lying excited states in ^{140}Ce. In this mass region, low-lying excitations for the odd-even nuclei exhibit excitations with a large single-particle component, while the corresponding even-even systems show strong collectivity and significant pairing.

Transition charge densities of the low-lying excited states are compared to the prediction of the quasiparticle-phonon model (QPM) [13–15], which has been successfully applied to the description of contributions of one- and two-phonon configurations to the transition charge densities of low-lying states in the $N=82$ region [7–9]. Our results are also compared with calculations from a self-consistent are also compared with calculations from a self-consistent finite Fermi system (FFS) theory using a modified version of the density functional.

II. EXPERIMENTAL PROCEDURE

A. MIT–Bates data

The data for this experiment were obtained at the high-resolution facility of the MIT–Bates Linear Accelerator Center. The 900 MeV/c energy-loss spectrometer system (ELSSY) [16] was used in a mode allowing a solid angle of 3.3 msr and a momentum bite of $\pm 3\%$. The beam energy was varied in the range of 100–370 MeV. Average currents of 25–35 μA were used. Beam current was monitored with an accuracy of 0.1% using the signals from two toroids fed into integrating amplifiers.

The focal plane was instrumented with two vertical drift chambers, the first of which was positioned approximately at the focal surface, two transverse arrays connected in series, two Čerenkov detectors, and the associated readout electronics [17]. The instrumentation is located outside of the spectrometer vacuum and is separated from the spectrometer vacuum by a thin Kevlar-reinforced Mylar window [18].

This experiment used ^{140}Ce targets with thicknesses of 4.97 and 22.85 mg/cm^2, isotopically enriched to 99.7%. Additional data were taken on either BeO or BeAl, ^{12}C, and ^{142}Ce to establish focal-plane parameters and energy calibrations using differential recoil from the various nuclides, and to measure background. The ^{12}C targets were also used to establish normalizations.

The scattering angle ranged from 40° to 101°, corresponding to a range of effective momentum transfer $q_{\rm eff}$ $[=q(1+3Ze^2/2ER)]$ between 0.4 and 2.5 fm^{-1}, where q is the elastic momentum transfer, E is the incident energy, and R is the nuclear rms radius. One additional measurement was performed at 155° and at a beam energy of 190 MeV ($q_{\rm eff}=2.0$ fm^{-1}) to investigate the transverse contribution to the form factor.

As part of the current experiment, effort was devoted to a continuing program of energy-resolution enhancement, primarily through studies of beam-tuning systematics and data-acquisition software refinement. This program resulted in attaining maximum resolutions of $\Delta p/p=4\times10^{-5}$ and routinely gave 6×10^{-5}. This was essential for studying an excitation region with many closely neighboring states.

B. Saclay data

The data were collected in the HE1 experimental hall of the ALS (Accelerateer Lineare de Saclay). Scattered electrons were analyzed using the SP900 magnetic spectrometer [19]. The standard focal-plane detector of this spectrometer was employed, which consists of a vertical drift chamber, two plastic scintillator planes, and a Čerenkov counter. The energy-loss system STRADIVARIUS [20] was used to obtain high resolution at high beam currents. For the optimum momentum resolution (typically $\Delta E/E=1\times10^{-4}$) the scattering chamber was connected directly to the spectrometer without intervening vacuum windows employing a sliding seal. The spectrometer acceptance solid angle ranged from 0.1 to 5.0 msr.

The beam current, which varied from 5 to 15 μA, was measured to an accuracy of better than 1% by two ferrite-core toroid monitors and a Faraday cup. The scattering of the incident electrons with energies $E=200$, 300, and 500 MeV was measured for a range of scattering angles θ corresponding to effective momentum transfers $0.4\le q_{\rm eff}\le 3.1$ fm^{-1}.

Errors due to the nonuniformity of the target thickness were minimized and excessive heating of the target was avoided by continuously wobbling the targets relative to the beam. Additional cooling of the target was provided by a supersonic jet of hydrogen gas directed at the beam spot. The relative efficiencies of the detector channels were checked by measurement of the smooth quasielastic spectrum from ^{12}C. The stability of the detector system was examined periodically by measurement of the ^{140}Ce elastic-scattering cross section at a forward angle.

III. DATA REDUCTION

A. Extraction of cross sections

Cross sections were extracted from the experimental spectra using a line-shape fitting code. A typical experimental spectrum and an associated line shape for the Bates data is shown in Fig. 1. The peak integrals extracted from the spectra were corrected for straggling, bremsstrahlung, and Schwinger radiative effects according to the prescription of Bergstrom [21]. In addition, on-line diagnostic spectra were accumulated so that corrections could be applied to compensate for the misidentification of good events and instrumental deadtime. For forward angle data, these corrections were normally of the order of a few percent and dominated by the computer deadtime correction. At backward angles, where the counting rate is low, instrumental and computer deadtime is negligible and the correction is dominated by the subtraction of spurious background events. All the data were also corrected for folding over the spectrometer acceptance and for multiple scattering in the target. The resulting cross sections were analyzed simultaneously with previous measurements [10] at low-momentum transfers. The inelastic cross sections were determined relative to the simultaneously measured elastic-scattering cross sections. Absolute cross sections were obtained by normalizing these data using the results of a high-precision elastic-

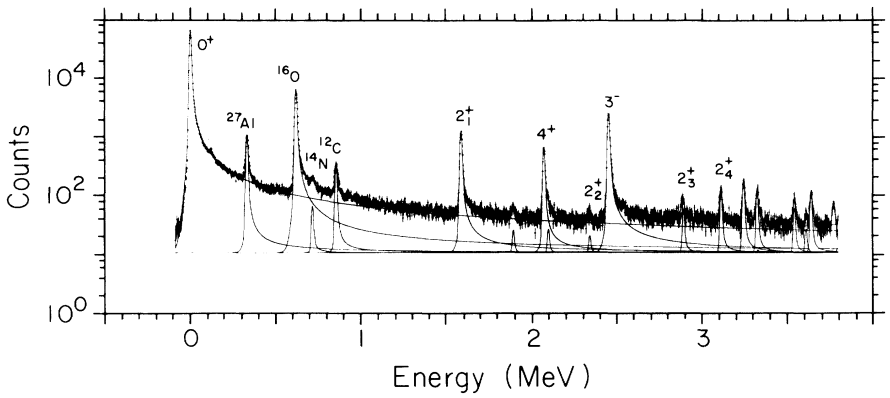

FIG. 1. Spectrum and line-shape fit of 190-MeV electrons scattered from ^{140}Ce at 45°.

electron-scattering experiment performed at Saclay [22].

The backward angle measurement showed that the transverse contributions to the form factor at forward angles are negligible. The ratios in $|F^T|^2/|F^C|^2$, where F^T and F^C are the transverse and longitudinal form factors, respectively, were observed to be 1.2% for the 2_1^+ state ($E_x=1.596$ MeV) and 4.0% for the 3_1^- state ($E_x=2.464$ MeV). This result is in accord with the recent NIKHEF electron-scattering results [7,8] on ^{142}Nd. At the forward angles corresponding to the first minimum of the longitudinal form factor ($q_{\text{eff}}=1.0$ fm^{-1}), the transverse components of the cross section for the quadrupole states of ^{142}Nd were measured to be less than 2% of the longitudinal form factor. Calculations with QPM have shown that the transverse form factors of all the quadrupole states reach their maximum value near the minimum of the charge form factor. For the states of other multipolarities in ^{142}Nd, QPM calculations [8] predict the transverse contribution to be of the same order as for the quadrupole states. We will therefore neglect the small transverse components of the natural parity ^{140}Ce states in the subsequent analysis.

B. Transition charge densities

Cross sections extracted from the electron-scattering spectra were analyzed using a distorted-wave Born approximation (DWBA) phase-shift code [23]. A Fourier-Bessel expansion (FBE) of transition densities was used to extract structure information from the experimental cross sections. The FBE expands densities as a series of spherical Bessel functions. The expansions used within a cutoff radius R_0 are

$$\rho(r)=\sum_{\mu=1}^{15} A_\mu q_\mu^{L-1} j_L(q_\mu^{L-1} r) , \tag{1}$$

$$J_{L,L+1}(r)=\sum_{\mu=1}^{15} B_\mu j_{L+1}(q_\mu^L r) , \tag{2}$$

$$J_{L,L}(r)=\sum_{\mu=1}^{15} C_\mu j_L(q_\mu^L r) , \tag{3}$$

where $q_\mu^L R_0$ is the μth zero of $j_L(x)$. The lower component of the current $J_{L,L-1}$ is related to the upper component and the charge through the continuity equation [23]. For the densities in ^{140}Ce we have used a cutoff radius $R_0=10.00$ fm. The data determine the coefficients up to that q_μ^L which is closest to $q_{\max}$, the maximum momentum transfer covered by the data. The remaining coefficients are determined by fitting additional pseudodata points in the region $q_{\max}\le q\le q_{15}^L$ with an uncertainty determined by an exponential upper limit as discussed in Ref. [23]. Model dependence enters through the use of an exponential tail bias in coordinate space. The tail bias ensures that the shape of the density is reasonable at large radii.

IV. THEORETICAL DESCRIPTION OF LOW-LYING NUCLEAR EXCITATIONS

In this section we briefly outline the two microscopic models we have used here for interpreting the experimental data, the quasiparticle-phonon model (QPM) and self-consistent finite Fermi system (FFS) theory. The self-consistent FFS theory employs a modified form of the density functional, from which both the quasiparticle basis and the effective interaction are constructed with a single fixed set of parameters for different nuclei. However, this theory in its present realization does not treat in detail the interplay between different modes of excitation. This interplay is taken into account within the QPM, a phenomenological approach in which the quasiparticle basis is obtained from the Woods-Saxon average field and a schematic form of the residual interaction is employed with parameters adjusted to the experimental data for each nucleus.

A. Quasiparticle-phonon model

In the quasiparticle-phonon model, the excited states in even-even nuclei are viewed as a combination of one-, two-, . . . , n-phonon configurations built on the wave function of the ground state $\Psi_{\text{g.s.}}$ treated as a phonon vacuum. In the present calculation up to three phonon configurations are included. Thus, the wave function of the state with momentum J and projection M has the form

$$\Psi_\nu(JM)=\left\{\sum_i R_i(J\nu)Q^\dagger_{JMi}+\sum_{LiL'i'}P^{L'i'}_{Li}(J\nu)[Q^\dagger_{L\mu i}Q^\dagger_{L'\mu'i'}]_{JM}\right.$$
$$\left.+\sum_{LiL'i'}\sum_{J'L''i''}T^{J'L''i''}_{LiL'i'}(J\nu)[[Q^\dagger_{L\mu i}Q^\dagger_{L'\mu'i'}]_{J'M'}Q^\dagger_{L''\mu''i''}]_{JM}+\cdots\right\}\Psi_{\text{g.s.}}\ , \tag{4}$$

with the definition

$$[Q^\dagger_{L\mu i}Q^\dagger_{L'\mu'i'}]_{JM}\equiv\sum_{\mu\mu'}\langle L\mu L'\mu'|JM\rangle Q^\dagger_{L\mu i}Q^\dagger_{L'\mu'i'}\ , \tag{5}$$

where $Q^\dagger_{L\mu i}$ is the phonon creation operator with angular momentum L, projection μ, and the RPA root number i. Phonons are constructed as a linear combination of pairs of quasiparticle creation $\alpha^\dagger_{jm}$ and annihilation α_{jm} operators with the shell quantum numbers $jm\equiv|n,l,j,m\rangle$ as follows:

$$Q^\dagger_{L\mu i}=\tfrac{1}{2}\sum_{jj'}^{N,Z}\{\psi^{Li}_{jj'}[\alpha^\dagger_{jm}\alpha^\dagger_{j'm'}]_{L\mu}$$
$$+(-1)^{L-\mu}\phi^{Li}_{jj'}[\alpha_{jm}\alpha_{j'm'}]_{L-\mu}\}\ . \tag{6}$$

After the diagonalization of the Hamiltonian on the basis of the wave function (4), the set of eigenvalue equations is obtained. Solving these equations we obtain a spectrum of excited states and the contributions of different configurations [i.e., coefficients $R_i(J\nu)$, $P^{L'i'}_{Li}(J\nu)$, and $T^{J'L''i''}_{LiL'i'}(J\nu)$] to the structure of each state. A detailed description can be found in Refs. [7–9].

B. Self-consistent finite Fermi system theory

In a companion paper [9] the transition charge densities of one-phonon states in ^{142}Ce were calculated using a simplified version of the FFS theory [4,5]. In that paper a single-particle basis in the Woods-Saxon potential and density-dependent effective interaction were used when solving QRPA-type equations in the coordinate representation. Contrary to the QPM, these calculations were characterized by the completeness of the particle-hole basis and a more realistic effective interaction.

In the present paper we apply a new version of the FFS theory which allows us to describe both ground and excited states self-consistently. For this purpose we used a density functional approach in a form close to that which was suggested in Ref. [24]. The corresponding interaction energy density is represented as a sum of four terms, omitting for simplicity the usual kinetic energy term with the bare nucleon mass,

$$\varepsilon_{\text{int}}=\varepsilon_{\text{main}}+\varepsilon_{\text{Coul}}+\varepsilon_{\text{sl}}+\varepsilon_{\text{pair}}\ , \tag{7}$$

where

$$\varepsilon_{\text{main}}=\tfrac{2}{3}\epsilon^0_F\rho_0[a^v_+x^2_+f^v_++a^v_-x^2_-f^v_-+a^s_+x_+\widetilde{f^s_-x_+}$$
$$+a^s_-x_-\widetilde{f^s_-x_-}]\ . \tag{8}$$

Here $x_\pm=(\rho_n\pm\rho_p)/2\rho_0$, $\rho_{n(p)}$ is the neutron (proton) density, $2\rho_0$ is the equilibrium nuclear matter density ($N=Z$), ϵ^0_F is the nuclear matter Fermi energy, and

$$f^v_\pm=\frac{1-h^v_{1\pm}x_+}{1+h^v_{2\pm}x_+},\quad f^s_\pm=\frac{1}{1+h^s_\pm x_+}\ , \tag{9}$$

$$\widetilde{f^s_\pm x_\pm}=\int D(\mathbf{r}-\mathbf{r}')f^s_\pm(\mathbf{r}')x_\pm(\mathbf{r}')d\mathbf{r}'\ , \tag{10}$$

$$D(\mathbf{r}-\mathbf{r}')=\delta(\mathbf{r}-\mathbf{r}')-\frac{1}{4\pi R^2|\mathbf{r}-\mathbf{r}'|}\exp\left[\frac{-|\mathbf{r}-\mathbf{r}'|}{R}\right]\ . \tag{11}$$

The first and second terms of $\varepsilon_{\text{main}}$ are the contributions of the volume isoscalar and isovector interaction energy. The last two terms are generated by the surface finite-range density-dependent forces.

The energy density of the Coulomb interaction $\varepsilon_{\text{Coul}}$ is taken in the usual form, including the exchange part in the Slater approximation. The term ε_{sl} comes from the spin-orbit and velocity spin-dependent interactions. The term $\varepsilon_{\text{pair}}$ is the pairing energy density generated by simple δ-function effective particle-particle forces.

Parameters of the density functional ($a^v_\pm$, $a^s_\pm$, $h^v_{1,2\pm}$, $h^s_\pm$, etc.) were chosen by fitting excitation energies, charge distributions, and the single-particle spectra for a number of nuclei, both magic (^{40}Ca, ^{48}Ca, ^{208}Pb) and nonmagic (^{90}Zr, ^{146}Gd, tin, and lead even-even isotopes). The results of these calculations will be published elsewhere [25].

A self-consistent quasiparticle basis and effective interactions, obtained with this functional, are used when solving the FFS equations for one-phonon excitations in a mixed (r,λ) representation, fully taking into account the particle-hole continuum as in Refs. [9,26].

V. RESULTS

The experimental spectra were analyzed up to an excitation energy of 3.3 MeV. Table I lists the excitation energies with spin and parity for all of the states analyzed [27]. The excitation energies and the $B(E\lambda)$ values of the low-lying states with different J^π obtained in the present experiment are presented in this table along with corresponding QPM calculations and self-consistent FFS predictions. Table II presents the properties of low-lying states in QPM calculations. This table gives the results in QPM with a one-phonon approximation and after mixing between the one-phonon, two-phonon, and three-phonon states. The two main configurations of the wave function after mixing are shown in this table for each state.

The coefficients presented in the last column of Table II correspond to R, P in Eq. (4). The contribution of each configuration to the structure of excited states can be obtained from the normalization relation

TABLE I. The excitation energies and the $B(E\lambda)$ values of the low-lying states with different J^π obtained from experiment, along with corresponding QPM calculations and self-consistent FFS predictions.

	Experiment		QPM		FFS	
J^π	E_x (MeV)	$B(E\lambda)$ ($e^2\text{fm}^{2\lambda}$)	E_x (MeV)	$B(E\lambda)$ ($e^2\text{fm}^{2\lambda}$)	E_x (MeV)	$B(E\lambda)$ ($e^2\text{fm}^{2\lambda}$)
2^+	1.596	$(3.04\pm0.08)\times10^3$	1.62	3.60×10^3	1.61	2.5×10^3
	2.348	$(4.3\pm2.8)\times10^1$	2.25	3.75×10^1		
	2.900	$(1.71\pm0.27)\times10^2$	3.05	3.87×10^2		
	3.119	$(6.59\pm0.51)\times10^2$	3.36	4.42×10^2		
3^-	2.464	$(1.98\pm0.14)\times10^5$	2.27	1.48×10^5	2.44	1.9×10^5
4^+	2.084	$(3.41\pm0.44)\times10^6$	2.08	3.61×10^6	1.96	2.0×10^6

$$\langle\Psi_\nu(JM)|\Psi_\nu(JM)\rangle=\sum_i[R_i(J\nu)]^2+2\sum_{LiL'i'}[P_{Li}^{L'i'}(J\nu)]^2\bar{K}^J(LiL'i')+6\sum_{LiLi'}\sum_{J'L''i''}[T_{LiL'i'}^{J'L''i''}(J\nu)]^2C_{J'}^J(Li,L'i',L''i'')=1\ , \tag{12}$$

where $\bar{K}^J(LiL'i')$ and $C_{J'}^J(Li,L'i',L''i'')$ are the coefficients related to the Pauli principle correction. The $\bar{K}^J(LiL'i')$ value in this equation varies from 1 to 0; 1 for the two-phonon configuration which does not violate the Pauli principle and 0 for the configuration which is forbidden by the Pauli principle. In ^{140}Ce the two-phonon configurations $[2_1^+\otimes3_1^-]_{3^-}$, $[2_1^+\otimes4_1^+]_{2^+}$, and $[2_1^+\otimes4_1^+]_{4^+}$ have the smallest values of the coefficient $\bar{K}^J(LiL'i')$. For some configurations this coefficient can be easily calculated by comparing the P value in the Table II with the contribution in percent described in this chapter.

A. 2^+ states

Four 2^+ states at excitation energies 1.596, 2.348, 2.900, and 3.119 MeV have been observed and analyzed in this experiment. Figure 2 shows the form factors and the corresponding DWBA fits for these 2^+ states. Figure 3 presents the empirically reconstructed transition charge densities of these 2^+ states. In this (and the following figures) we compare to the experimental densities obtained in the QPM calculations (solid curves) and those obtained by FFS theory calculations (dashed curves). The states at 1.596 and 3.119 MeV are characterized by

TABLE II. Properties of low-lying states with $J^\pi=2^+$, 3^-, and 4^+ and $E_x\le4$ MeV in ^{140}Ce in QPM calculations: (a) in the one-phonon approximation with the wave function in Eq. (6); (b) in calculations after mixing between the one-, two-, and three-phonon states with the wave function in Eq. (4) (only two main configurations of wave function are shown for each state).

		(a)		(b)		
J^π	ν	E_x (MeV)	$B(E\lambda)$ ($e^2\text{fm}^{2\lambda}$)	E_x (MeV)	$B(E\lambda)$ ($e^2\text{fm}^{2\lambda}$)	Main configurations
2^+	1	1.82	3.54×10^3	1.62	3.60×10^3	$0.95Q^+_{2^+_1}+0.09[Q^+_{3^-_1}Q^+_{3^-_1}]_{2^+}$
	2	2.36	1.04×10^0	2.25	3.75×10^1	$0.68Q^+_{2^+_2}+0.68Q^+_{2^+_3}$
	3	2.39	2.05×10^1	2.31	1.37×10^0	$0.70Q^+_{2^+_2}-0.70Q^+_{2^+_3}$
	4	3.46	1.60×10^3	3.05	3.87×10^2	$0.72Q^+_{2^+_4}+0.39[Q^+_{2^+_1}Q^+_{2^+_1}]_{2^+}$
	5			3.36	4.42×10^2	$0.50Q^+_{2^+_4}-0.50[Q^+_{2^+_1}Q^+_{2^+_1}]_{2^+}$
	6			3.88	2.20×10^2	$0.38Q^+_{2^+_4}-0.81[Q^+_{2^+_1}Q^+_{4^+_1}]_{2^+}$
3^-	1	2.80	1.85×10^5	2.27	1.48×10^5	$0.90Q^+_{3^-_1}+0.38[Q^+_{2^+_1}Q^+_{3^-_1}]_{3^-}$
	2	3.44	4.52×10^1	3.31	7.15×10^2	$0.97Q^+_{3^-_2}+0.14[Q^+_{2^+_1}Q^+_{3^-_2}]_{3^-}$
4^+	1	2.16	3.10×10^6	2.08	3.61×10^6	$0.97Q^+_{4^+_1}+0.14Q^+_{4^+_2}$
	2	2.35	6.58×10^4	2.29	1.65×10^2	$0.89Q^+_{4^+_2}+0.21Q^+_{4^+_3}$
	3	2.40	7.63×10^4	2.35	5.89×10^3	$0.96Q^+_{4^+_3}-0.24Q^+_{4^+_2}$
	4	3.81	3.96×10^6	3.14	6.92×10^5	$0.53Q^+_{4^+_4}+0.50[Q^+_{2^+_1}Q^+_{2^+_1}]_{4^+}$
	5			3.36	1.02×10^6	$0.56Q^+_{4^+_4}-0.42[Q^+_{2^+_1}Q^+_{2^+_1}]_{4^+}$
	6			3.80	1.58×10^5	$0.86[Q^+_{2^+_1}Q^+_{4^+_1}]_{4^+}-0.42[Q^+_{2^+_1}Q^+_{6^+_1}]_{4^+}$

surface-peaked transition densities that indicate their collective nature.

The first 2^+ state, at an excitation energy of $E_x = 1.596$ MeV, has a strong surface peak with the maximum at 5.7 fm. In the QPM calculation the 2_1^+ state is expected to have excitation energy of 1.62 MeV and $B(E2) = 3.6 \times 10^3\ e^2\,\mathrm{fm}^4$. The position and amplitude of the experimental density are well reproduced, although the amplitude of the interior peak is overestimated by theory. The nature of this interior peak is connected with the contribution of the $(\pi 2d_{5/2})^2_{2+}$ two-quasiparticle configuration to the structure of the first one-phonon 2^+ configuration, which is the main configuration (91% of contribution) in the wave function of the 2_1^+ state. The same feature characterizes calculations concerning the neighboring even-even isotopes ^{142}Ce (Ref. [9]) and ^{142}Nd (Refs. [7,8]). The contribution of the $(\pi 2d_{5/2})^2_{2+}$ two-quasiparticle configuration to the structure of the first one-phonon 2^+ configuration in ^{140}Ce is 25% smaller than in ^{142}Nd; consequently, the height of the interior peak compared to the surface peak appears reduced. This contribution in ^{140}Ce is larger than in ^{142}Ce. In ^{142}Ce it is equal to 15% because of additional neutron contributions.

The surface peaks for collective states are produced as a result of coherent interference of a large number of two-quasiparticle components, while in the interior the interference is mainly destructive, and as a result the density behavior in the interior is usually determined by one or two main proton two-quasiparticle configurations.

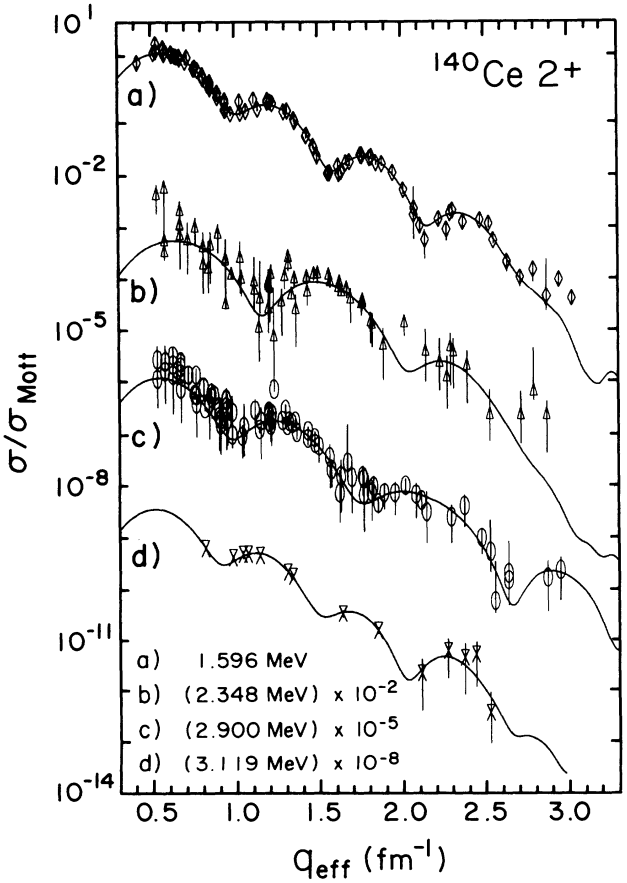

FIG. 2. Form factors for the 2^+ states at 1.596, 2.348, 2.900, and 3.119 MeV. The curves show the DWBA fits.

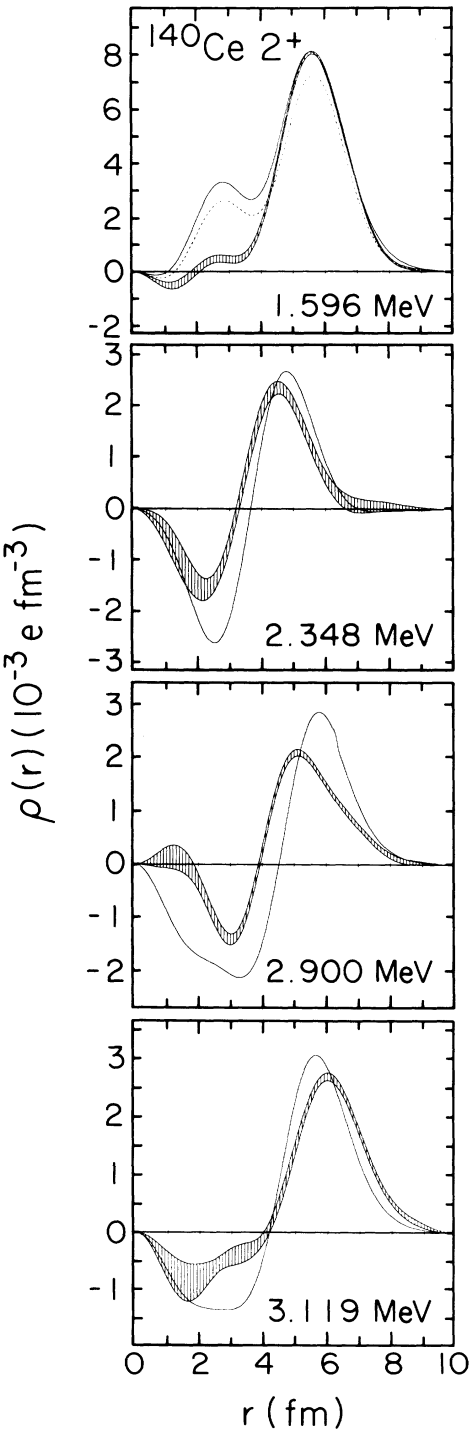

FIG. 3. Transition charge densities for the 2^+ states at 1.596, 2.348, 2.900, and 3.119 MeV. The solid curves are the QPM calculations, while the dashed curve is the self-consistent FFS prediction.

The uncertainties in details of both approaches (QPM and FFS theory), such as the single-particle energy scheme, should be expected to produce a worse description of the experimental densities in the interior than at the surface.

The self-consistent FFS calculation for the first 2^+ state gives an excitation energy of 1.61 MeV and $B(E2)=2.5\times10^3\ e^2\text{fm}^4$. The corresponding transition charge density is shown in Fig. 3 by a dashed curve. In principle, by varying some parameters of the density functional one can bring the surface peak and $B(E2)$ value much closer to the experiment. For example, it may be done by increasing the absolute value of parameter a^v_+, i.e., the attraction between nucleons, and by readjusting the strength constants of the spin-orbit and pairing interactions. We prefer to hold all parameters, as obtained from the fitting procedure mentioned above, constant. The contribution to $B(E2)$ from the interior part of the transition density is small, and the influence of the variations of the density functional on this part is much less pronounced.

The second and third 2^+ states of ^{140}Ce in the QPM calculation are superpositions of the two noncollective configurations (the second and third one-phonon 2^+ modes). These two one-phonon 2^+ configurations are closely spaced in energy, being located at 2.355- and 2.388-MeV excitation, which results in substantial mixing. The amplitudes of these configurations add constructively in the second 2^+ state at 2.25 MeV, giving a $B(E2)=3.8\times10^1\ e^2\text{fm}^4$, while they interfere destructively in the third 2^+ state at 2.31 MeV, producing a $B(E2)$ of only 1.4 $e^2\text{fm}^4$. The transition charge density of the second QPM 2^+ state exhibits a pronounced node in the interior, indicating its noncollective nature. It resembles closely the shape of the experimental density of the 2^+_2 state at 2.348 MeV (Fig. 3). Three configurations comprise the 2^+_2 state; $(\pi 1g_{7/2},\pi 2d_{5/2})_{2^+}$ (61.5%), $(\pi 1g_{7/2})^2_{2^+}$ (30.0%), $(\pi 2d_{5/2})^2_{2^+}$ (8.5%). The large negative peak in the interior is caused by the first configuration. The third 2^+ state in the QPM is expected to be very weak; this state is not observed in our experiment, nor is there any other evidence for such a state at the present time.

The shape of the densities of the fourth and fifth 2^+ states in the QPM calculation is determined mainly by the contribution of the fourth one-phonon 2^+ configuration to the wave function of these states. The fourth one-phonon 2^+ configuration is rather collective. While the strength of the first one-phonon 2^+ configuration is mainly concentrated in the first 2^+_1 state, the strength of the fourth one-phonon 2^+ configuration is distributed over several states. 52% of its strength goes to the fourth 2^+ state at 3.05 MeV with $B(E2)=3.9\times10^2\ e^2\text{fm}^4$ and 25% goes to the fifth 2^+ state at 3.36 MeV with $B(E2)=4.4\times10^2\ e^2\text{fm}^4$. The smaller value of $B(E2)$ of the fourth 2^+ state compared to the fifth is caused by a 2.5% destructive admixture of the first 2^+ one-phonon configuration to the wave function of the fourth 2^+ state. Also, a visible contribution to the structure of the fourth and fifth 2^+ states comes from the two-phonon configuration $[2^+_1\otimes 2^+_1]_{2^+}$, 30% and 50%, respectively. In Fig. 3, the shape and amplitude of the fourth state in QPM are compared with the experimental density of the 2^+ state at 2.900 MeV. While the extracted density for the level at 2.900 MeV does have an interior maximum indicative of its noncollective nature, the absolute positions of the peaks are not well reproduced by the QPM calculation. However, both the shape and amplitude of the density of the fifth state in QPM are in good agreement with the experimental density of the 2^+ collective state at 3.119 MeV.

Quite remarkable is the measured and predicted high collectivity of the fifth-calculated, fourth-observed 2^+_4 state at an excitation energy of 3.119 MeV. This is a manifestation of the fact that the $1g_{7/2}$ and $2d_{5/2}$ energy levels are closely spaced, while the $1h_{11/2}$, $3s_{1/2}$, and $2d_{3/2}$ orbitals are a few MeV higher. This strong collective 2^+_4 state was also observed in ^{142}Nd (Ref. [7]), and was explained in terms of the single-particle subshell structure.

B. 4^+ state

The form factor and the transition charge density for the first 4^+ state (2.084 MeV) are presented in Figs. 4 and 5, respectively. In ^{142}Nd the transition charge density of the first 4^+ state has not been extracted since this state is located very close to the first 3^- state and their peaks were not resolved [7,8]. In ^{140}Ce these states are well separated.

The 4^+_1 state in the QPM calculation appears at 2.08 MeV with a $B(E4)=3.6\times10^6\ e^2\text{fm}^8$, and it is essentially a pure first one-phonon 4^+ configuration. The first one-phonon 4^+ configuration is less collective than the first one-phonon 2^+ and 3^- configurations. More than 96% of its strength comes from the three two-quasiparticle configurations $(\pi 1g_{7/2})^2_{4^+}$ (53.8%), $(\pi 1g_{7/2},\pi 2d_{5/2})_{4^+}$

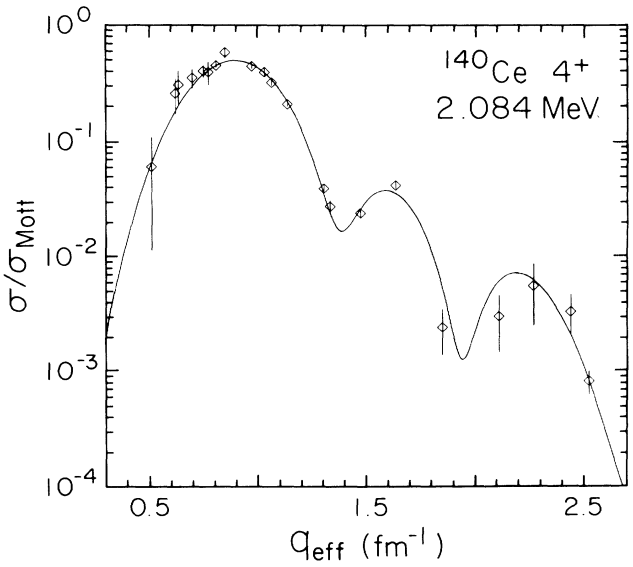

FIG. 4. Form factor for the 4^+ state at 2.084 MeV.

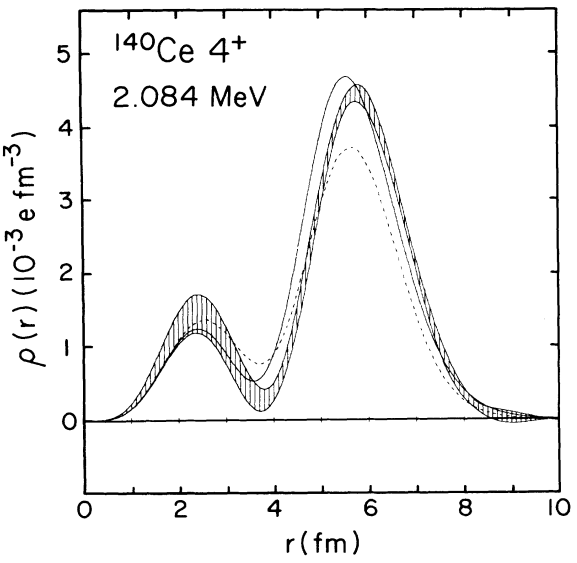

FIG. 5. Transition charge density for the 4^+ state at 2.084 MeV. The solid curve is the QPM calculation, while the dashed curve is the self-consistent FFS prediction.

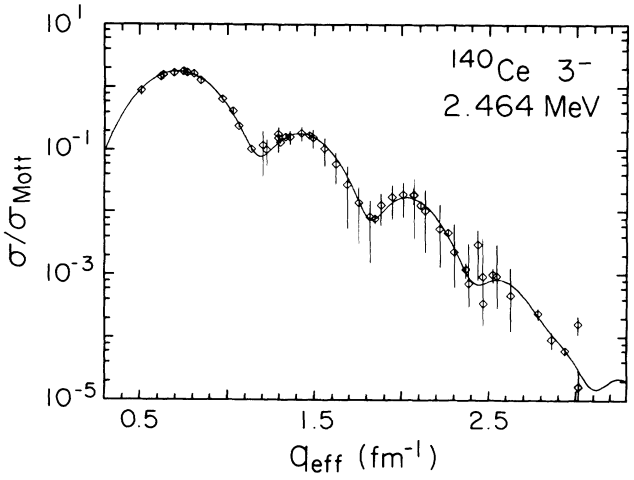

FIG. 6. Form factor for the 3^- state at 2.464 MeV.

(29.4%), and $(\pi 2d_{5/2})^2_{4^+}$ (13.1%). The smaller degree in collectivity of this first one-phonon 4^+ configuration is the main reason for the weak coupling of this configuration to more complex ones. In general, the agreement of the QPM results with the experiment is rather good both in terms of excitation energy and in terms of the shape of its transition density.

For the 4^+_1 state the self-consistent FFS calculation gives $E_x = 1.96$ MeV and $B(E4) = 2.0 \times 10^6\ e^2\,\mathrm{fm}^8$. The shape of the transition charge density for this state is reproduced rather well, but the width and the height of the surface peak are underestimated. This can be explained by the relative lack of collectivity of this state, which makes it more sensitive to positions of single-particle levels near the Fermi surface than the first 2^+ state. As mentioned earlier no attempt was made to improve the agreement with experiment by varying the density functional parameters.

C. 3^- state

The form factor and the transition charge density of the first 3^- state at an excitation energy of 2.464 MeV are shown in Figs. 6 and 7, respectively. The 3^-_1 state in the QPM calculation is found at 2.27 MeV with a $B(E3)$ of $1.5 \times 10^5\ e^2\,\mathrm{fm}^6$. The main contribution (80.3%) to the structure of this state comes from the first one-phonon 3^- configuration with a 12.9% admixture from the two-phonon configuration $[2^+_1 \otimes 3^-_1]_{3^-}$. Although the two-quasiparticle configuration $(\pi 2d_{5/2}, \pi 1h_{11/2})_{3^-}$ contributes 68% to the structure of the first one-phonon 3^- configuration, the one-phonon configuration is rather collective; it exhausts 5.7% of the energy-weighted sum rule.

In the QPM calculation for ^{140}Ce, the $(\pi 1g_{7/2}, \pi 1h_{11/2})_{3^-}$ two-quasiparticle configuration is found to lie lower in energy than the $(\pi 2d_{5/2}, \pi 1h_{11/2})_{3^-}$ configuration by only 0.05 MeV. However, since the $(\pi 2d_{5/2}, \pi 1h_{11/2})_{3^-}$ configuration has a matrix element of residual interaction 3.5 times larger than the $(\pi 1g_{7/2}, \pi 1h_{11/2})_{3^-}$ configuration, its contribution to the first 3^- state is larger.

The self-consistent FFS theory calculation gives an excitation energy for the first 3^- of 2.44 MeV with a $B(E3) = 1.9 \times 10^5\ e^2\,\mathrm{fm}^6$. The corresponding transition charge density is shown in Fig. 7 by a dashed curve. The agreement with experiment is good. In this approach for negative-parity excitations, uncertainties connected with

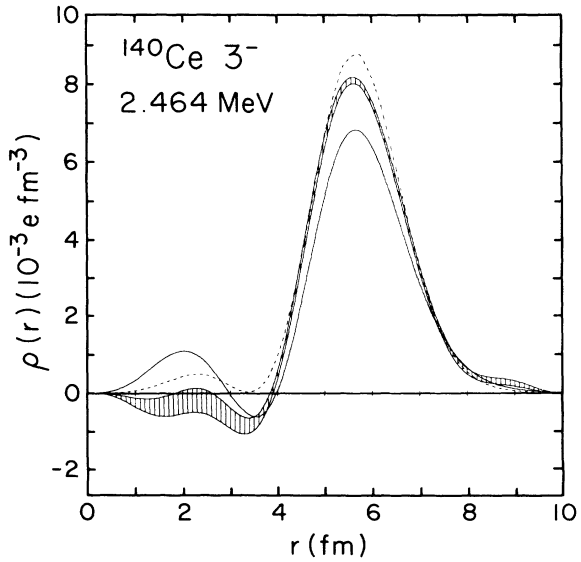

FIG. 7. Transition charge density for the 3^- state at 2.464 MeV. The solid curve is the QPM calculation, while the dashed curve is the self-consistent FFS prediction.

particle-particle channel contributions are diminished because the QRPA-type equations [26] do not explicitly include the corresponding anomalous component of the transition density. At the same time the particle-hole channel, which in this case plays the most important role, is adequately taken into account.

VI. SUMMARY AND CONCLUSIONS

In this experiment, electron-scattering cross sections for the low-lying states of ^{140}Ce have been measured for excitation energies up to 3.3 MeV. The excellent energy resolution made it possible to separate the form factors of the low-lying states for the first time. For six of these states, accurate transition charge densities were reconstructed by means of a DWBA analysis using a Fourier-Bessel expansion. For these levels, spin and parity assignments were confirmed. A systematic investigation of the modes of excitation of low-lying states was performed.

In this work, special attention has been given to the interplay between single-particle and collective degrees of freedom. To this end, the experimental results were compared with calculations in the framework of the quasiparticle-phonon model and finite Fermi system theory. The QPM calculations, with many phonon configurations contributing to the wave functions of excited states, made it possible to analyze the structure of the extracted states. The self-consistent FFS theory proves to be quite successful in a description of the first excited collective states of each multipolarity, which have a dominantly one-phonon character. As for the higher-lying states, it was found that the mixing with more complicated configurations needs to be taken into account. This mixing can be described microscopically with the framework of FFS theory, and the corresponding calculation scheme is being developed now.

In general, the agreement between the experimentally extracted transition charge densities and the theoretical calculations in both the frequency of the excited states and the shape of the corresponding transition charge densities in the surface region is quite good. The poorer description of the interior structure of the densities is attributed to the destructive nature of the interference, which is more sensitive to the details of the calculations which have not reached that level of maturity yet. A comparison of ^{140}Ce with ^{142}Ce indicates that the two additional neutrons above the closed shell $N=82$ strongly increase the interplay between different components in the wave functions of excited states. In the open-shell nucleus ^{142}Ce, the interaction between one-, two-, and three-phonon components is rather strong [9]. Due to this interaction, one- and two-phonon configurations are mixed in the wave function of the excited states, and only the first 2^+ state can be approximated by a pure one-phonon state. In the half-magic nucleus ^{140}Ce the mixing is much weaker and the one-phonon approximation of the FFS is reasonable. This conclusion is reinforced by the fact that the results in ^{140}Ce are very similar to those of the neighboring half-magic ^{142}Nd with two more protons in the open shell.

The study of these nuclei, together with the more extensive studies in the Zr-Sr and Pb regions, indicates that while we do not yet have a precise calculational framework to represent the features of nuclei with the accuracy achieved by experimental technique, we do have a good understanding of how their features develop as each shell is opened from the magic nucleus, and we do have the calculational framework to reproduce their gross features rather satisfactorily.

ACKNOWLEDGMENTS

We would like to thank the staff at the MIT–Bates Linear Accelerator Center and Saclay for their efforts in giving us the high-quality beams and support necessary for this experiment. This work was supported, in part, by the Department of Energy through Contract No. DE-AS02-79ER10338 and the National Science Foundation through Grant No. NSF PHY 86-10493.

[1] D. Goutte, J. B. Bellicard, J. M. Cavedon, B. Frois, M. Huet, P. Leconte, Phan Xuan Ho, S. Platchkov, J. Heisenberg, J. Lichtenstadt, C. N. Papanicolas, and I. Sick, Phys. Rev. Lett. **45**, 1618 (1980); J. Heisenberg, J. Lichtenstadt, C. N. Papanicolas, and J. S. McCarthy, Phys. Rev. C **25**, 2292 (1982).

[2] G. F. Bertsch and S. F. Tsai, Phys. Lett. **50B**, 319 (1974); Phys. Rep. **18C**, 125 (1975); J. Decharge and D. Gogny, Phys. Rev. C **21**, 1568 (1980).

[3] V. A. Khodel, Pis'ma Zh. Eksp. Teor. Fiz. **16**, 410 (1972) [JETP Lett. **16**, 291 (1972)]; **18**, 126 (1973) [**18**, 72 (1973)]; Yad. Fiz. **19**, 792 (1974) [Sov. J. Nucl. Phys. **19**, 404 (1974)].

[4] S. A. Fayans, V. A. Khodel, and E. E. Saperstein, Nucl. Phys. **A317**, 424 (1979).

[5] V. A. Khodel and E. E. Saperstein, Nucl. Phys. **A348**, 261 (1980).

[6] O. Schwentker, J. Dawson, J. Robb, J. Heisenberg, J. Lichtenstadt, C. N. Papanicolas, J. Wise, J. S. McCarthy, L. T. van der Bijl, and H. P. Blok, Phys. Rev. Lett. **50**, 15 (1983).

[7] R. K. J. Sandor, H. P. Blok, U. Garg, M. N. Harakeh, C. W. de Jager, V. Yu. Ponomarev, A. I. Vdovin, and H. de Vries, Phys. Lett. B **233**, 54 (1989); R. K. J. Sandor, H. P. Blok, U. Garg, M. N. Harakeh, C. W. de Jager, V. Yu. Ponomarev, A. I. Vdovin, and H. de Vries, Nucl. Phys. **A535**, 669 (1991).

[8] R. K. J. Sandor, Ph.D. thesis, Vrije Universiteit Te Amsterdam, 1991.

[9] W. Kim, J. R. Calarco, J. P. Connelly, J. H. Heisenberg, F. W. Hersman, T. E. Milliman, J. E. Wise, B. L. Miller, C. N. Papanicolas, V. Yu. Ponomarev, E. E. Saperstein, and A. P. Platonov, Phys. Rev. C **44**, 2400 (1991).

[10] R. Pitthan, Z. Naturforsch. **25**, 13510 (1970).

[11] A. Richter, in *Proceedings of the International Conference on Nuclear Physics with Electromagnetic Interactions*, Mainz, 1979, edited by Arenhövel and Dreschsel.

[12] B. L. Miller, L. S. Cardman, C. N. Papanicolas, T. E. Mil-

liman, J. P. Connelly, J. H. Heisenberg, F. W. Hersman, J. E. Wise, B. Frois, D. Goutte, and V. Meot, Phys. Rev. C **37**, 895 (1988).
[13] V. G. Soloviev, *Theory of Complex Nuclei* (Pergamon, Oxford, 1976).
[14] A. I. Vdovin and V. G. Soloviev, Fiz. Elem. Chastits At. Yadra **14**, 237 (1983) [Sov. J. Part. Nucl. **14**, 99 (1983)].
[15] V. V. Voronov and V. G. Soloviev, Fiz. Elem. Chastits At. Yadra **14**, 1380 (1983) [Sov. J. Part. Nucl. **14**, 583 (1983)].
[16] W. Bertozzi, M. V. Hynes, C. P. Sargent, W. Turchinetz, and C. Williamson, Nucl. Instrum. Methods **162**, 211 (1979).
[17] W. Bertozzi, M. V. Hynes, C. P. Sargent, C. Cresswell, P. C. Dunn, A. Hirsh, M. Seitch, B. Norum, F. N. Rad, and T. Sasanuma, Nucl. Instrum. Methods **141**, 457 (1977).
[18] F. W. Hersman, Ph.D. thesis, MIT, 1982.
[19] P. Leconte *et al.*, Nucl. Instrum. Methods **169**, 401 (1980).
[20] C. Grunberg and P. Leconte (unpublished).
[21] J. Bergstrom, in *MIT 1967 Summer Study, Medium Energy Nuclear Physics with Electron Accelerators,* edited by W. Bertozzi and S. Kowalski (MIT, Cambridge, MA, 1967), p. 251.
[22] D. Goutte *et al.* (unpublished).
[23] J. Heisenberg, Adv. Nucl. Phys. **12**, 61 (1981); S. E. Koonin, *Computational Physics* (Benjamin/Cummings, New York, 1986), p. 112.
[24] A. V. Smirnov, S. V. Tolokonnikov, and S. A. Fayans, Yad. Fiz. **48**, 1661 (1988) [Sov. J. Nucl. Phys. **48**, 995 (1988)].
[25] S. A. Fayans (in preparation).
[26] A. P. Platonov and E. E. Saperstein, Nucl. Phys. **A486**, 63 (1988).
[27] L. K. Peker, Nucl. Data Sheets **51**, 425 (1987).